ORIGINAL RESEARCH ARTICLE

Slurry Jet Erosion Resistance of VC-Containing Tool Steels: the Role of the Carbide Volume Fraction

O.A. Zambrano ⓘ, Kidus Yoseph Tufa, and Jiaren Jiang

Tool steels are well known to have superior strength and are claimed to have superior wear resistance than conventional steels in several scenarios. However, their behavior under slurry erosion conditions have been seldom studied. To this end, a set of tool steels, primarily from the CPM yV (y = 1, 3, 9, 10, 15) alloy family, was selected to understand the effect of hardness and vanadium carbide content on the slurry jet erosion (SJE) performance at different impingement angles. It was observed that the SJE resistance increases with the increase in the vanadium carbide volume fraction, but is independent of alloy hardness.

1. Introduction

Slurry jet erosion (SJE) is a major issue for equipment that handles slurry. It results in significant costs due to failures, downtime and material replacement (Ref 1). SJE has been a persistent problem in industries such as mineral processing, hydrometallurgy, oil sands mining, slurry pumping, and pulp and paper manufacturing. Erosion caused by particulate material in the liquid leads to metal loss and represents a significant industrial challenge (Ref 2). In some operations, wear becomes a critical issue not only due to the high material cost related to severe wear loss but also because of the production interruptions as a result of scheduled or forced shutdowns. There are also cases where leaking of slurry being handled such as bitumen slurry (mixture of bitumen, sand and hot water) can have significant safety and environmental implications.

In terms of practical applications, choosing the right materials for a specific use is one of the best ways to reduce wear loss. Yet, material selection is a difficult challenge facing engineers in order to meet the complex needs of maintaining reliable production operation with the best economical outcomes. The best solution will thus be inevitably a best compromise between material performance and cost (material, fabrication, capital investment, maintenance, production interruptions, etc.). For example, in the oil sands operation, different materials have been used for different sections of the pipelines, including pipe steels and different stainless steel grades (Ref 3) or steel pipes lined with chromium carbide overlays (CCO), chromium white irons or elastomers. In mineral processing, materials for mill liners include chromium white irons, steels (martensitic, pearlitic, bainitic or austenitic high manganese) or rubbers. Obviously, it is highly valuable to expand options for engineers to choose from when dealing with particular wear situations.

Among the various materials, some tool steels have unique properties and may hold high potential for specific applications against wear by hard particles. Tool steels typically have a carbon content greater than 0.5%, and heat treatments on these steels can lead to achieve high levels of hardness and toughness. Some tool steels contain high concentrations of carbon and carbide formation alloying elements such as Cr, W and V, producing microstructures that are suited for resisting wear by hard particles. On the other hand, some engineering components have complicated shapes and/or require accurate dimensions and at the same time require good wear resistance. In such cases, conventional high-wear–resistant materials such as Cr white irons or hardfacing may not be very suitable due to the difficulties in fabrication or due to the lack of mechanical strength or toughness. An instance of this can be observed in the auto slurry samplers' sleeve that is employed in slurry transportation of oil sands. The primary constituents of the auto sampler encompass a cylindrical plunger, which features an elastomer ring on its outer diameter and slides within a sleeve. It is installed on the slurry pipeline wall. When activated, the plunger extracts a specific volume of slurry from the pipeline into the sleeve before discharging it into an external container. In order to guarantee an appropriate seal between the plunger and the sleeve, the sleeve must be precisely machined to the correct dimensions and it also requires high wear resistance.

Although tool steels may have high potentials for abrasion and/or slurry erosion applications, except for dry sand abrasion resistance (typically tested under the ASTM G65 conditions), very limited studies have been conducted on the wear behavior of tool steels in the literature. In the genre of tool steels, those with high vanadium content such as the CPM y V (y = 1, 3, 9, 10 and 15) alloy system may excel in diverse wear scenarios

O.A. Zambrano, Kidus Yoseph Tufa, and **Jiaren Jiang**, Mining Wear and Corrosion Laboratory, National Research Council Canada, 4250 Wesbrook Mall, Vancouver, BC V6T 1W5, Canada. Contact e-mail: oscar.zambrano@nrc-cnrc.gc.ca.

because of their fine microstructures, high attainable hardness and toughness through the crucible particle metallurgy (CPM) process. ASTM G65 (dry sand/rubber wheel) testing of laser clad CPM 9V, 10V and 15V tool on an AISI 1070 carbon steel showed that the CMP 15V clad has much better low-stress abrasion resistance than the other clads, and when compared with the bulk AISI D2 tool steel, the wear loss is reduced by about 86% (Ref 4). Under dry sliding wear conditions (Ref 5), laser clad of CPM 15V tool steel on a H13 hot working tool steel displayed a reduction in the wear volume loss by about 78% when compared with the base hardened H13 tool steel. In bulk, the CPM 10V tool steel has showed reductions in wear by about 81% when compared with AISI A2 and D2 tool steels under reciprocating ball-on-flat conditions (Ref 6). The wear resistance of CPM yV steels has been tested as well under pin abrasion test conditions after ion nitriding (Ref 7), showing benefits up to $\sim$ 80% as compared with the base tool steel. These steels have been evaluated as well for die repair applications (Ref 8); CPM 9V alloy has been applied to an H13 tool steel, and it was shown that hard vanadium carbides are responsible for a deposit hardness of 800 HV while in the base/substrate this value is about 200 HV. Moreover, it was found that the compressive residual stresses produced in cladding are beneficial for repair purposes because they hinder crack growth and improve the life span of the die. Finally, a recent work (Ref 9) reports the successful joining of CPM 15V tool steel onto low-carbon steel using the linear friction welding technology targeting wear applications.

Despite the studies mentioned earlier, the erosion wear behavior of these steels has not been yet addressed in the literature. In a recent paper (Ref 10), the present authors studied the Coriolis scouring erosion (very low impingement angles $\sim \leq 15°$) resistance of the CPM yV steels where it was observed that carbide volume fraction (CVF) has a direct relationship with scouring erosion wear. The role of erodent particle size, changing impingement angle from 20 to 90° and the CVF in tool steels is still unknown. The impingement angle is a crucial parameter that significantly influences the erosion rate under slurry jet erosion conditions. Understanding the effect of impingement angle is important as it can help the most appropriate use ofthese alloy. Slurry erosion is a severe problem and a major concern for slurry handling equipment, as it leads to considerable expense caused by failures, downtime and material replacement costs. Impingement angle is one of the most important parameters significantly affecting erosion rate in slurry jet erosion. Slurry erosion is a severe problem and a major concern for slurry handling equipment, as it leads to considerable expense caused by failures, downtime and material replacement costs. As stated recently by Javaheri et al. (Ref 2), one of the key research areas is to understand a possible transition in the target material from ductile to brittle behavior during the course of the erosion process which is a key factor. In particular, for tool steels, the impingement angle can have a significant effect on the erosion behavior and this effect has not been sufficiently studied in these materials. For example, one study found that slurry erosion was maximum at an impingement angle of 60° for a given steel, indicating a mixed mode of erosion (ductile as well as brittle) (Ref 11). By studying the effects of impingement angle on slurry jet erosion in tool steels, researchers can gain a better understanding of this complex failure mode and develop new test methodologies and erosion-resistant materials to minimize erosion rates.

In this work, to explore the potential of tool steels for industrial slurry handling applications, a group of five CPM xV

tool steels has been tested using the slurry jet erosion (SJE) testing method at different impingement angles. The results are compared with the performance of a typical ASTM A532 IIIA Cr white cast iron that is commonly used in the industry for slurry handling applications. The role of vanadium, vanadium carbide fraction and hardness on the slurry erosion behavior has been studied. Finally, it is important to note that these tool steels can be considered as two-phase materials (or inhomogeneous materials in the context of Zum Gahr's terminology (Ref 12)): a continuous matrix and carbides, which differ from the homogeneous ductile and brittle materials studied in classical papers related to erosion, such as those found in (Ref 13, 14).

2. Experimental Procedure

2.1 Materials

Five grades of tool steels: CPM 1 V, CPM 3 V, CPM 9 V, CPM 10 V and CPM 15 V were selected. The constituent elements of these alloys and their proportions, including the ASTM A532 IIIA Cr white cast iron, were provided by the producer and are shown in Table 1.

The alloys underwent heat treatment to achieve an optimal balance of hardness and toughness, and details of the heat treatment parameters are provided in (Ref 10). The Cr white cast iron was heat-treated according to proprietary procedures used in production by a reputable slurry pump manufacturer.

2.2 Electron Backscatter Diffraction (EBSD) Characterization

Detailed characterization of phases in the microstructures of the steels was conducted using electron backscatter diffraction (EBSD) technique. The steels were prepared using the standard metallographic preparation followed by a final polishing procedure what was carried out using a VibroMet 2 vibratory polisher with 0.04 μm un-crystallized colloidal silica for 14 h. Prior to being analyzed in the SEM, the samples were cleaned for 12 min using a plasma cleaner. The SEM was operated at 25 kV accelerating voltage with a current of 13 nA at a working distance of 16 mm using a step size of 0.20 μm between each point. The samples were tilted at 70°. The EBSD maps were analyzed and post-processed using the AZtecCrystal® software. Wild spikes and non-indexed points were corrected by considering the orientation of the neighboring pixels and averaging at least five of them.
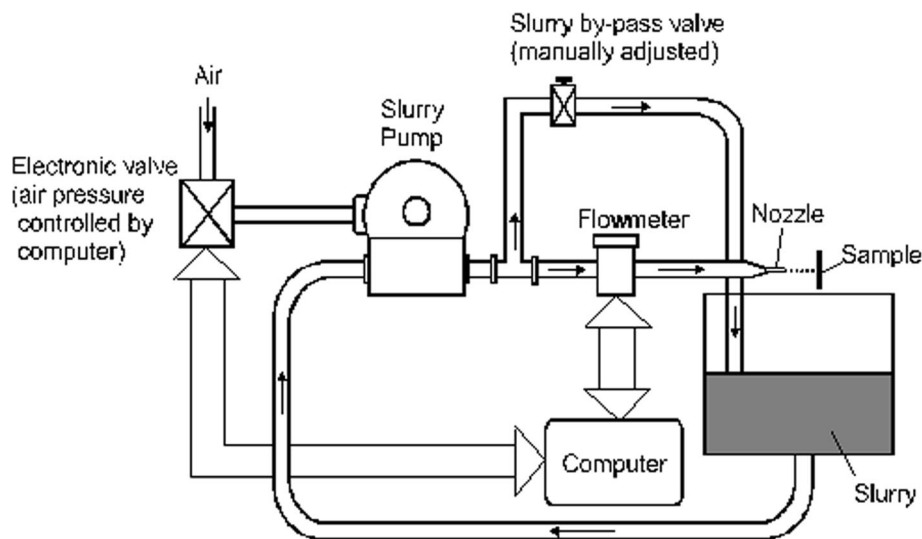
2.3 Slurry Jet Erosion Tests

Figure 1 shows schematically the slurry jet erosion tester used in the study. In this testing system, a slurry pump is used to circulate slurry from the slurry bath and to produce a slurry jet through a nozzle which impact on the surface of a static test specimen installed near the exit of the nozzle. A new batch of slurry is used for each test. Slurry velocity is controlled via a slurry flow meter and a closed loop control system.

The erosion tests were performed by means of a slurry composed of standard AFS 50–70 silica sand and water. The erodent's hardness ($HV_{1.96\ N}$) is 776 $\pm$ 124 (Ref 15). Before starting the experiment, 12 liters of water is added in the SJE tester slurry reservoir (Figure 1). Then the slurry pump is turned on to circulate the water and the flow rate is adjusted to the

Table 1 Chemical compositions of the studied alloys (wt.%)

Alloy	C	Cr	V	W	Mo	Mn	Ni	Fe
CPM 1 V	0.55	4.5	1	2.15	2.75	0.29	…	Balance
CPM 3 V	0.80	7.5	2.75	…	1.30	0.40	…	Balance
CPM 9 V	1.90	5.25	9.10	…	1.30	0.50	…	Balance
CPM 10 V	2.45	5.25	9.75	…	1.30	0.50	…	Balance
CPM 15 V	3.40	5.25	14.50	…	1.30	0.40	…	Balance
ASTM A532 IIIA Cr WI	2.9	27.2	…	…	0.08	0.98	0.8	Balance

Fig. 1 Illustration of the slurry jet erosion testing apparatus

desired value (18.6 lpm). While the water is recirculating, 1200 g of AFS 50-70 silica sand is slowly added to the slurry bath to obtain a well-dispersed homogenous slurry with a concentration of 10% wt. The slurry jet has a velocity of 16 m/s upon impacting the test sample surface. The slurry velocity of 16 m/s used here is on the higher end of slurry flow among different industrial applications. Such relatively high slurry flow can be encountered in slurry pumps and some hydro-cyclones. But in most slurry pipelines (oil sands, mineral processing), the typical slurry velocity is in the neighborhood of 5 m/s. The use of 16 m/s was a based on the combined consideration of industrial relevance and the reliable laboratory testing accuracy for accessing a broad range of industrial materials. Results obtained at this velocity using the AFS 50-70 silica sand (∼250 μm) can be translated to slurry erosion at lower velocities with larger erodent particles. The orifice diameter of the nozzle is 5 mm, and the standoff distance of the nozzle from the test specimen is 100 mm. The SJE test was conducted with a slurry temperature of 22°C and a test duration of 2 hours. The tests were conducted at three different impingement angles: 20°, 45° and 90°. Each condition was tested twice, resulting in a total of 30 tests. Error bars in the charts represent ± one standard deviation.

To remove any imperfections and the decarburization layer generated during heat treatment, 500 μm was ground off the test samples. The dimensions of the specimens are as follows: 25.4 ± 0.5 mm x 76.2 ± 2 mm x 12.7 mm ± 6 mm. Specimen surfaces are ground with a surface finish better than roughness

average (Ra) 0.6 μm. The volume loss was determined employing a Viking Solarius Development laser profilometer. The samples were scanned at a scan speed of 5 mm/s with 15 μm resolution in the X and Y directions, and the data have been processed using the Solarius Development SolarMap 5.1 software. The volume loss was determined by first leveling the non-worn flat surface area which is performed after excluding the worn surface area. The leveled non-worn area is used as a zero reference.

2.4 Hardness and Impact Toughness Measurements

A Rockwell C apparatus (NewAgeIndentron NI400C) was used to determine the hardness of the heat-treated samples. The reported results are the average of at least six indentations for each material along with the corresponding standard deviation. Vickers scale hardness equivalent was converted from the measured HRC hardness according to the ASTM E140 standard (Ref 16).

The impact toughness of the CPM yV steels was determined using Charpy V-notch testing at − 40°C employing specimens of 10 mm x 10 mm x 55 mm size, three coupons per steel; the striker radius is 8 mm. The specimens were cooled in a liquid bath (ASTM E23 paragraph 8.2.4.1). The specimen temperature is measured by using a dummy specimen that has an attached thermocouple and is immersed in the liquid bath together with the specimens to be tested. The liquid bath is cooled by the addition of liquid nitrogen until the thermocouple

Table 2 Results of VC carbide size, CVF (%), mean free path, hardness and impact toughness (Charpy) of the CPM yV tool steels

Alloy	CVF, %	VC size, μm	Mean free path, λ, μm	Hardness (HRC)	Equivalent harness HV (Ref 16)	Charpy V-notch test at − 40°C, Joules
CPM 1V	5.1	1.63 ± 0.36	11.6	60.3 ± 0.5	704	6.4 ± 2.9
CPM 3V	11.1	1.87 ± 0.43	7.2	60.3 ± 0.5	697	7.2 ± 2.8
CPM 9V	15.6	2.22 ± 0.31	5.6	55.4 ± 0.6	582	6.9 ± 3.1
CPM 10V	17.1	2.94 ± 0.64	4.9	60.3 ± 0.5	676	5.2 ± 2.8
CPM 15V	24.4	4.65 ± 0.70	4.6	60.9 ± 0.3	718	4.7 ± 2.5
ASTM A 532 IIIA WCI	31.5	…	…	60.1	701	…

on the dummy specimen indicates that the test temperature has been reached. This temperature is maintained for a minimum 5 minutes, and then, the test specimens are taken out from the bath, one at a time, and tested as quickly as possible.

2.5 Wear Scar Analysis

The wear scar analysis was conducted using secondary electrons (SE) (EDT detector) and backscattered electrons (T1 detector) at a voltage of 20 kV and a beam current of 3.2 nA on an Apreo 2S SEM (ThermoFisher).

3. Results

3.1 Microstructure and Properties

The optical micrographs and the methodology for measuring the carbide volume fraction (CVF), including the CVF and mean free path values, have been reported previously in (Ref 10). All specimens were found to have a tempered martensite microstructure with globular VC and a small amount of retained austenite. The VC carbide particle size, carbide volume fraction (CVF), mean free path, hardness and Charpy impact energy for each steel are shown in Table 2. As anticipated, an increase in the vanadium content leads to an increase in CVF.

In this study, microstructures of the different tool steels have been further examined using EBSD, including the determination of phase fractions (austenite, martensite and VC). EBSD micrographs of the CPM 1V, CPM 3V, CPM 9V and CPM 15V tool steels are shown in Figure 2, 3, 4, 5 and 6, respectively. In these EBSD analysis results, the blue, red and green colors represent the γ, α' and VC phases, respectively, and the boundaries with misorientations (θ) satisfying $1° \leq \theta < 15°$ were classified as low-angle grain boundaries (LAGBs) (Ref 17–19). The corresponding summary information from each of these EBSD maps is shown in Figure 2(d), 3(d), 4(d), 5(d) and 6(d), including distribution of crystallographic orientation and volume fractions of the different phases. It can be clearly seen that there is no preferred crystallographic orientation among the CPM yV tool steels.

For the martensite phase identification, either b.c.c. or b.c.t can be used. The main difference is basically on the c-axis, which is longer for b.c.t (α') than for b.c.c (α) due to the distortion created by interstitial carbon. Given the fact that the martensite reported here was resulted from a triple tempering treatment (Ref 10), the excessive interstitial carbon causing the c-axis distortions should have been rejected during the

tempering. It is thus reasonable to index the martensite as b.c.c crystal structure rather than b.c.t. The quantitative phase analysis results for the different CPM yV steels are summarized in Table 3. In general, the percentage of retained austenite among the CPM yV steels is very low. The amounts of detected austenite (f.c.c crystal structure) in the CPM 1V and CPM 15V steels are 0.6% and 0.4%, respectively, which can be considered to be within the indexation error. The CPM 9V steel contained about 4.4% retained austenite which is the highest among all the studied CPM yV tool steels. This steel was designed mainly for higher-shock/impact resistance applications where the CPM 10V steel was not tough enough. It has considerably lower hardness than the other CPM yV tool steels (Table 2). This higher retained austenite in CPM 9V may have been related to its specific different alloying strategy from the rest of the CPM yV family tool steels.

The VC (space group: Fm3m) and austenite (space group: Fm3m) crystal structures are very similar under EBSD indexation, and the main difference is the lattice parameter of 4.159 Å and 3.63 Å for the VC and austenite, respectively. Therefore, in some regions, particularly at the interface between the VC and temperate martensite, the small retained austenite detected could be a misindexation of the VC. It is important to point out that the differences found between the CVF reported in Table 2 and those obtained here by using EBSD can be attributed to the differences in methods and techniques. Results reported in Table 2 are more statistically meaningful since they were obtained using larger areas (Ref 10), while the EBSD is a representative of a particular region of the microstructure at 2000x.

The misorientation of the grains is shown in Figure 2(c), 3(c), 4(c), 5(c) and 6(c) through the grain orientation spread (GOS) with the distribution values reported in Figure 2(d), 3(d), 4(d), 5(d) and 6(d). The miscrostructure among the CPM yV tool steels showed very low misorientation values, which is related to the low density of geometrical necessary dislocations (GNDs) (Ref 20), and hence, there is a very low degree of stress/strain fields acting in the analyzed microstructure, such as in the case of a recrystallized microstructures (Ref 17–19, 21). This is somewhat expected due to the triple tempering treatment performed on these steels after the initial quenching (Ref 10), which will have annihilated most of the GNDs. In addition, this is also in alignment with the small percentages of retained austenite found in the CPM yV tool steels. The EBSD band contrast and the reconstructed austenitic parent phase images for the CPM 1V, 3V, 9V, 10V and 15V tool steels are provided in the supplementary information section (Figure S6, S7, S8, S9 and S10, respectively).
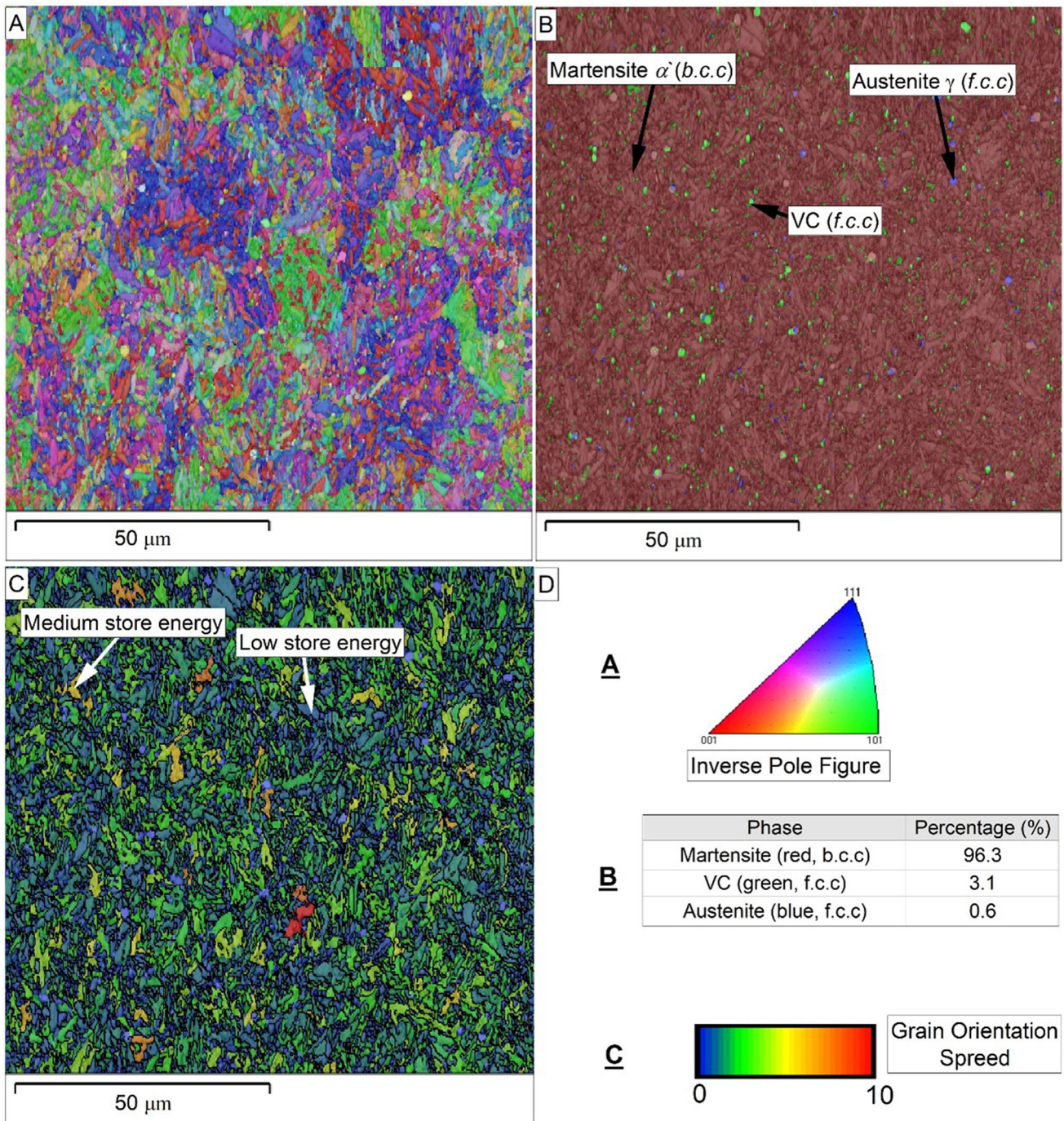
Fig. 2 EBSD maps of the CPM 1V tool steel initial microstructure where (a) is the inverse pole figure (IPF) map, (b) is the phase map, (c) is the GOS map (including grain boundaries of 15°), and (d) is relevant information to interpret the maps (a), (b) and (c)

3.2 Slurry Jet Erosion Tests

3.2.1 The Role of Impingement Angle. The variation of wear volume loss in the slurry jet erosion (SJE) test as a function of the impingement angle for the CPM yV steels is shown in Figure 7. Results for the ASTM A532 IIIA Cr white cast iron (CWI) are also presented for the purpose of comparison in Figure 7. Wear loss was the lowest at the low impingement angle of 20° for all the five studied steels and the CWI. The maximum wear loss was observed at 45° for CPM 1V, but appeared at the high impingement angle of 90° for

CPM 9V, 10V and 15V steels and CWI. For CPM 3V, wear loss was similar at 45° and 90°. It can be observed that the volume loss of CPM 9V-15V steels was substantially lower than the CWI.

It is generally known that maximum wear loss tends to occur at the low impingement angles (close to about 30°) for ductile materials while maximum wear loss appears at high impingement angles (90°) for brittle materials (Ref 13, 14, 22–25). Maximum wear loss at an angle close to 30° is attributed to the dominant microcutting mechanism for ductile materials while high wear loss at the high impingement angle is due to brittle
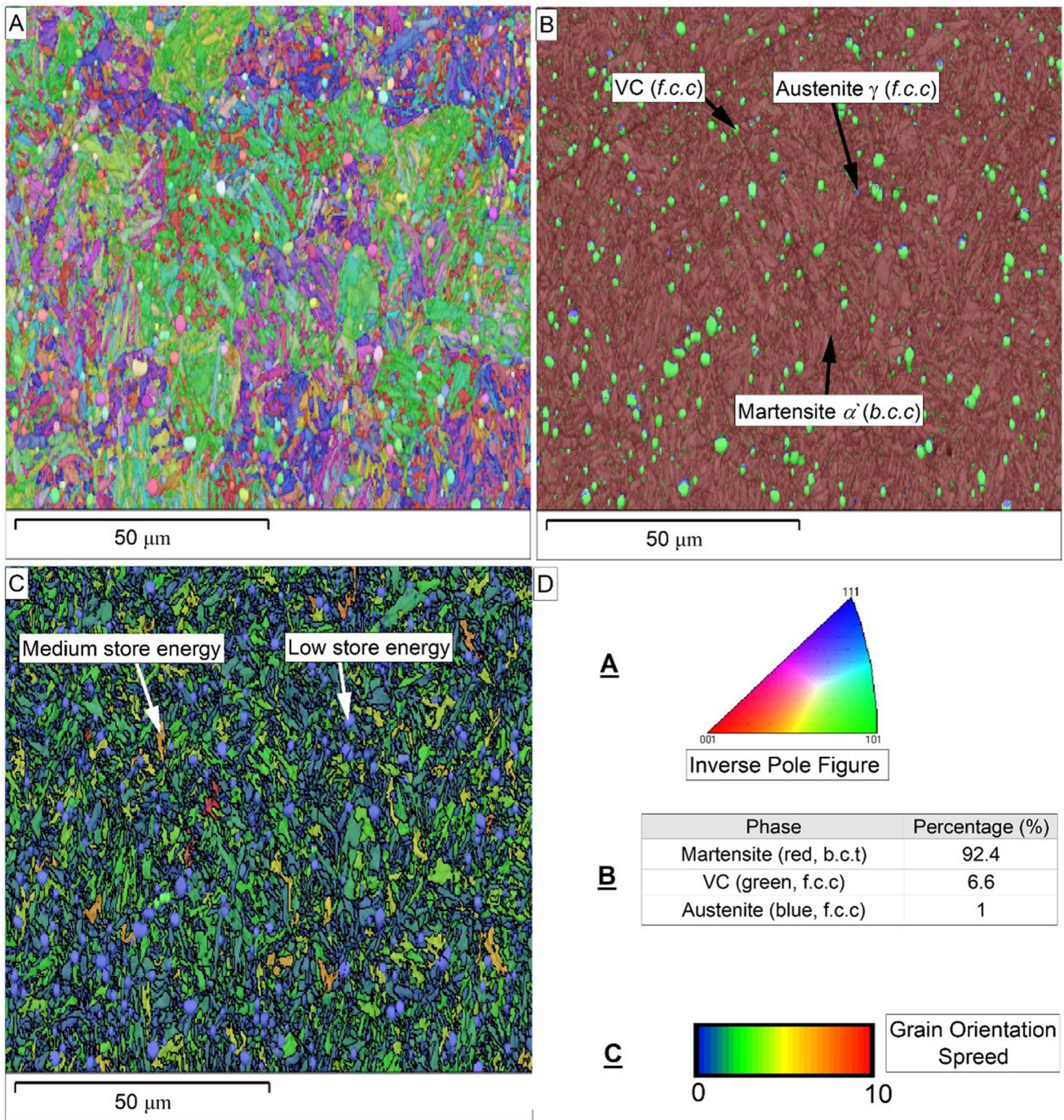
Fig. 3 EBSD maps of the CPM 3V tool steel initial microstructure where (a) is the inverse pole figure (IPF) map, (b) is the phase map, (c) is the GOS map (including grain boundaries of 15°), and (d) is relevant information to interpret the maps (a), (b) and (c)

microfracture. Although the current study only tested at three impingement angles, the general trend is reasonably clear. CPM 1V behaved more like a ductile material, with maximum wear close to the lower-angle end, while the high-V steels (CPM 9V, 10V and 15V) showed behavior closer to that for brittle materials, with the maximum wear loss shifting toward the high impingement angles. It should be pointed out that, since the tests were conducted at three impingement angles, the actual maximum wear loss for the high-V steels may have not been at 90°, but may have occurred at an angle somewhere between 45

and 90°. The behavior of CPM 3V can be described as semi-ductile, i.e., between ductile and brittle materials. The results in Figure 7 suggest that there may be a gradual ductile to brittle transition in the erosion behavior with the increase in the vanadium content or CVF for the different grades of steels.

Overall, an increase in the vanadium content or CVF leads to a decrease in the erosion volume loss, Figure 7, with CPM 15 exhibiting the lowest volume loss while CPM 1V being the one with the highest volume loss among the studied alloys. The increase is more apparent from CPM 1V to CPM 3V and from
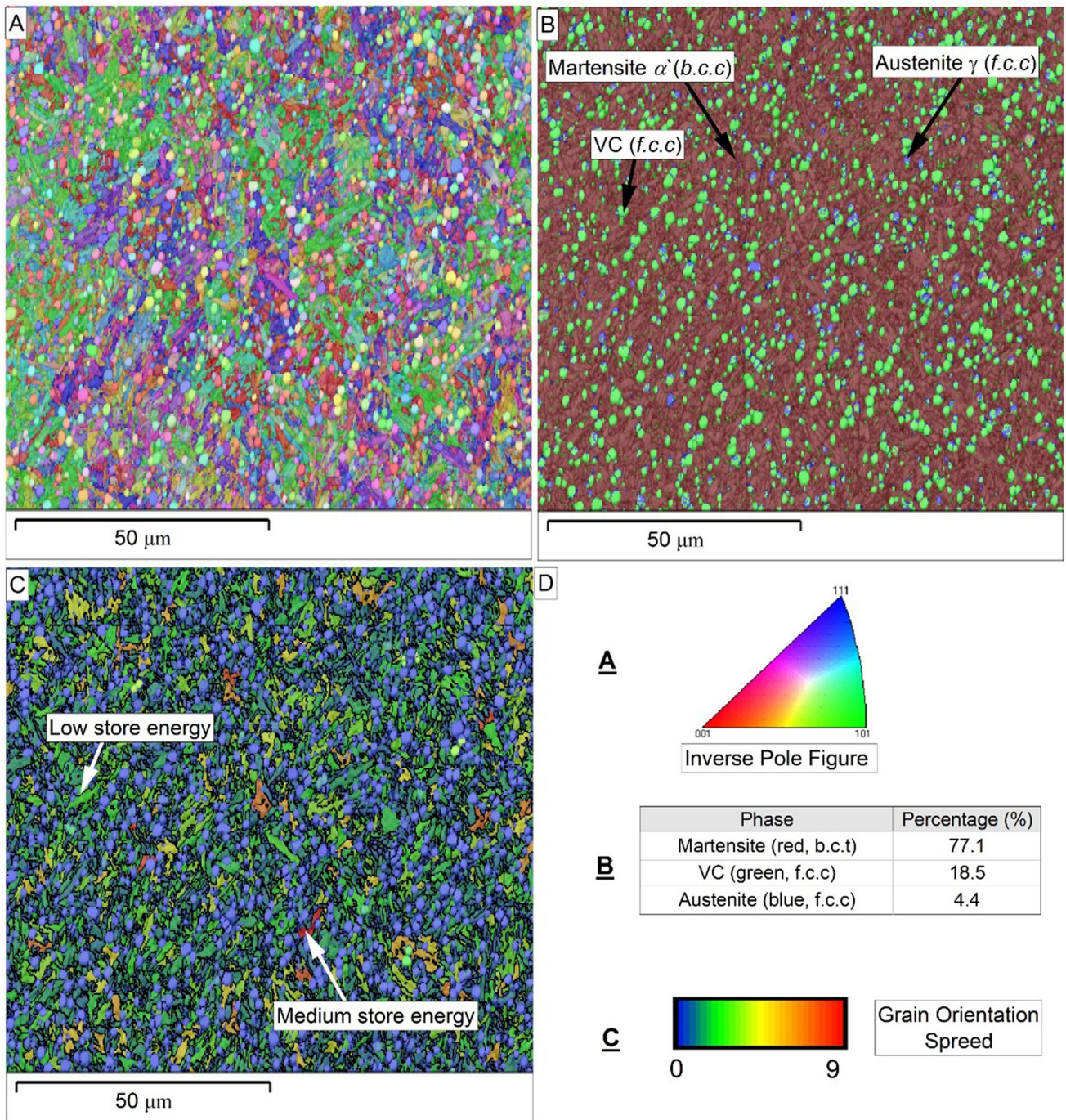
Fig. 4 EBSD maps of the CPM 9V tool steel initial microstructure where (a) is the inverse pole figure (IPF) map, (b) is the phase map, (c) is the GOS map (including grain boundaries of 15°), and (d) is relevant information to interpret the maps (a), (b) and (c)

CPM 3V to CPM 9V than that between CPM 9V, 10V and 15V. The effects of various factors contributing to these differences will be discussed further in the following sections.

3.2.2 The Role of Steel Hardness. Figure 8 shows the SJE wear loss versus steel hardness. No strong correlation between hardness and SJE resistance was found. Moreover, it is apparent that while CPM 1V and CPM 15V steels exhibit comparable levels of hardness, their wear resistance differs significantly. Therefore, it can be concluded that hardness alone does not dictate the SJE response in the studied conditions, and

other factors have been considered which will be discussed below. Comparable findings have been reported in previous studies when evaluating materials with equivalent levels of hardness in diverse tribological systems (Ref 10, 26).

In the literature on abrasive wear, hardness has been shown to be an important factor. Material wear resistance mostly depends on the ratio of the abrasive hardness (H_a) to the worn surface hardness (H_m), H_a/H_m, typically in a Z-shaped curve (Ref 12). In the intermediate values of the H_a/H_m ratio, the material loss rate increases significantly with increase in the H_a/H_m ratio (or in the material hardness). However, for very
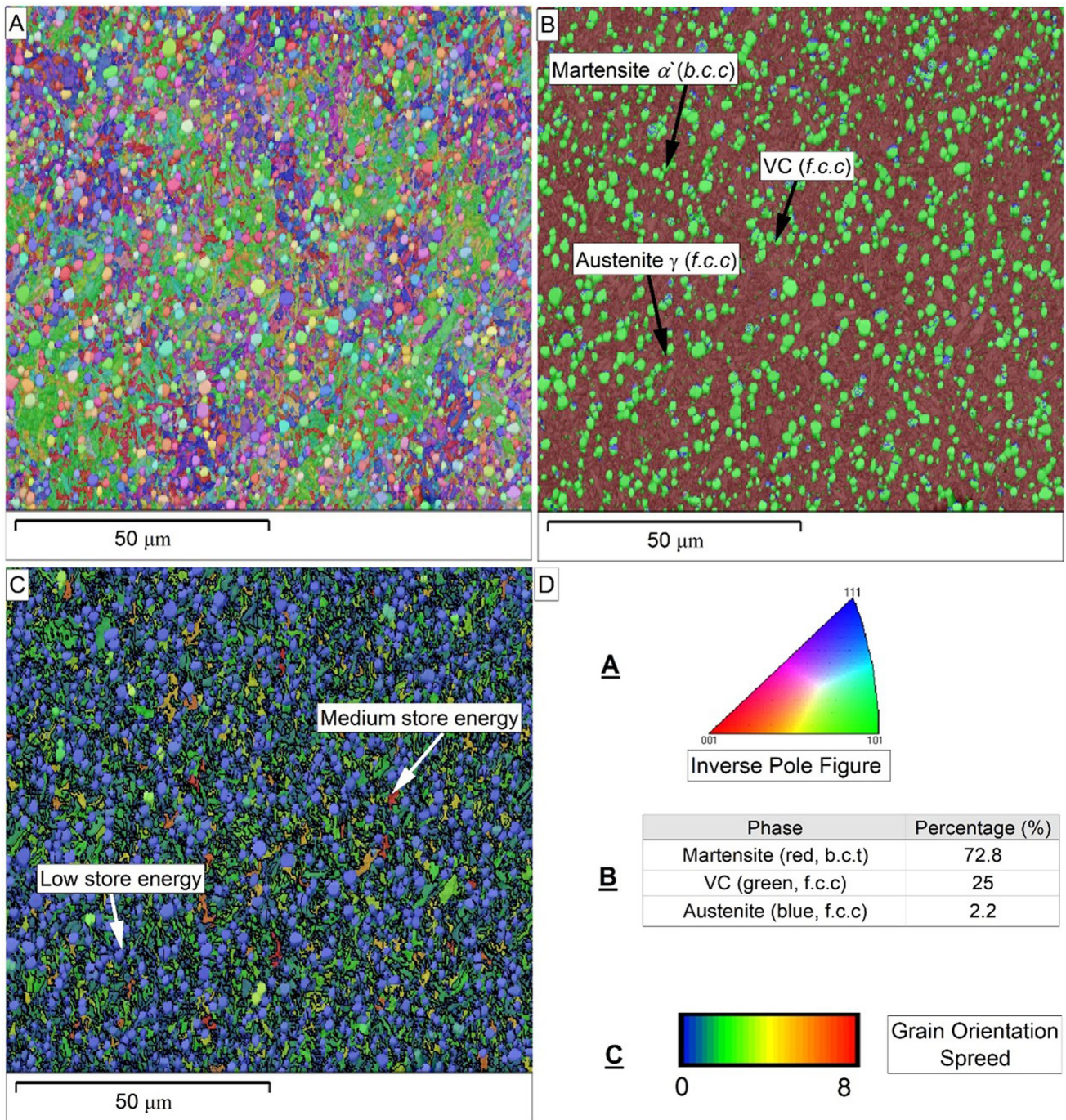
Fig. 5 EBSD maps of the CPM 10V tool steel initial microstructure where (a) is the inverse pole figure (IPF) map, (b) is the phase map, (c) is the GOS map (including grain boundaries of 15°), and (d) is relevant information to interpret the maps (a), (b) and (c)

hard or very soft materials, i.e., at H_a/H_m ratios below or above certain values, the effect of material hardness becomes negligible. The wear regimes are mild and severe wear for hard and soft materials, respectively. Please note that the "hard" or "soft" materials are relative to the hardness of the abrasive. For materials with homogeneous microstructures, the transition zone between mild and severe wear for H_a/H_m ratio is between about 1.0 and 1.2. On the other hand, materials with inhomogeneous microstructures such as those containing hard carbides usually have a softer matrix. The transition from the lower (mild) to the higher (severe) wear level occurs in a

broader range, e.g., between 0.8 and 1.6 (Ref 12), mostly depending on the hardness of the hard phase (the carbide).

Based on the hardness measurement results of the steels in Table 2 and assuming that silica sand has a hardness of 652–900 HV (See sect. 2.3), the hardness ratios, H_a/H_m, for the CPM yV steels are given in Table 4.

Apparently, the H_a/H_m values vary between 0.93 and 1.55 with an average of 1.16. This is right in the mid of the transition zone for inhomogeneous materials. According to the Z-curve (Ref 12) between wear rate and the H_a/H_m ratio, material hardness should have apparent effect on erosion rate. This is in
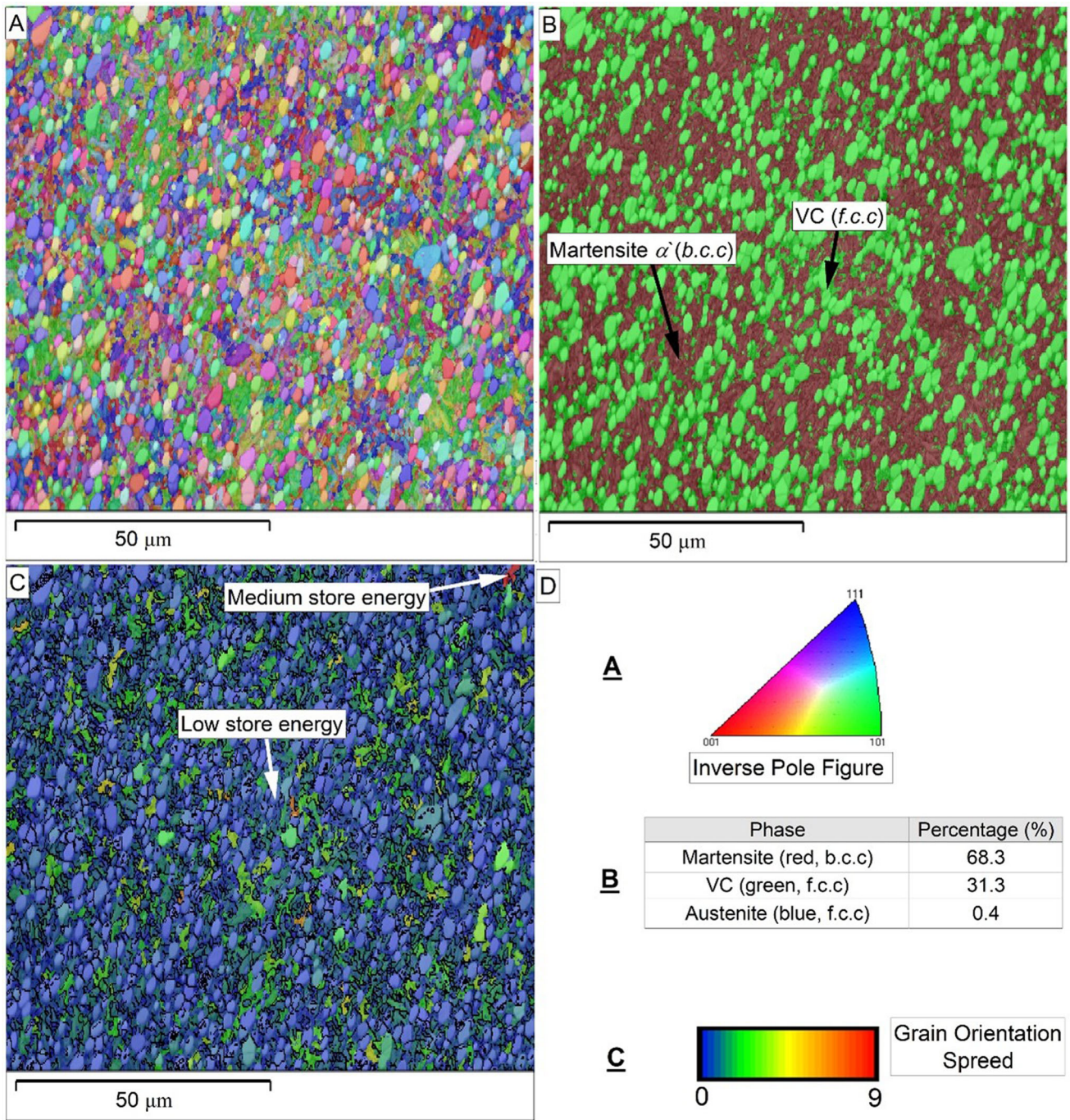
Fig. 6 EBSD maps of the CPM 15V tool steel initial microstructure where (a) is the inverse pole figure (IPF) map, (b) is the phase map, (c) is the GOS map (including grain boundaries of 15°), and (d) is relevant information to interpret the maps (a), (b) and (c)

Table 3 Summary of EBSD phase volume fraction (%) analysis for the CPM yV tool steels

Alloy	Tempered martensite, α, b.c.c	VC	Austenite, γ, f.c.c
CPM 1V	96	3.1	0.6
CPM 3V	92.4	6.6	1
CPM 9V	77.1	18.5	4.4
CPM 10V	72.8	25	2.2
CPM 15V	68.3	31.3	0.4
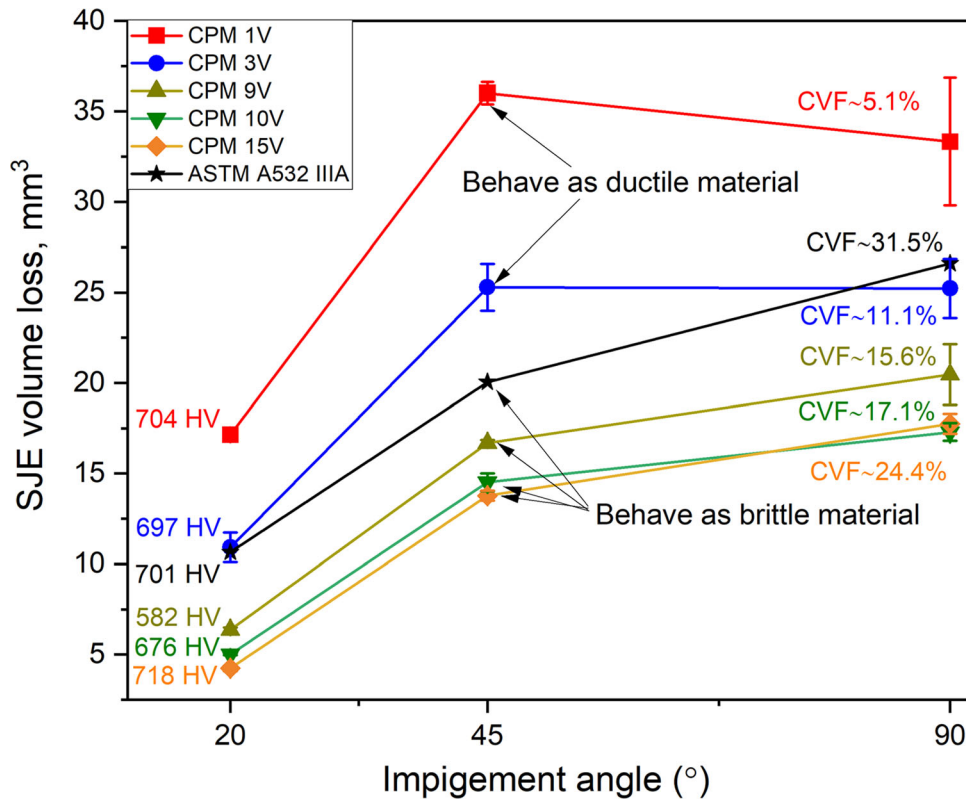
Fig. 7 Relationship between SJE wear volume loss (mm^3) and impingement angle (°) for the CPM yV tool steels and an ASTM A532 IIIA type Cr white cast iron. The CVF stands for carbide volume fraction.
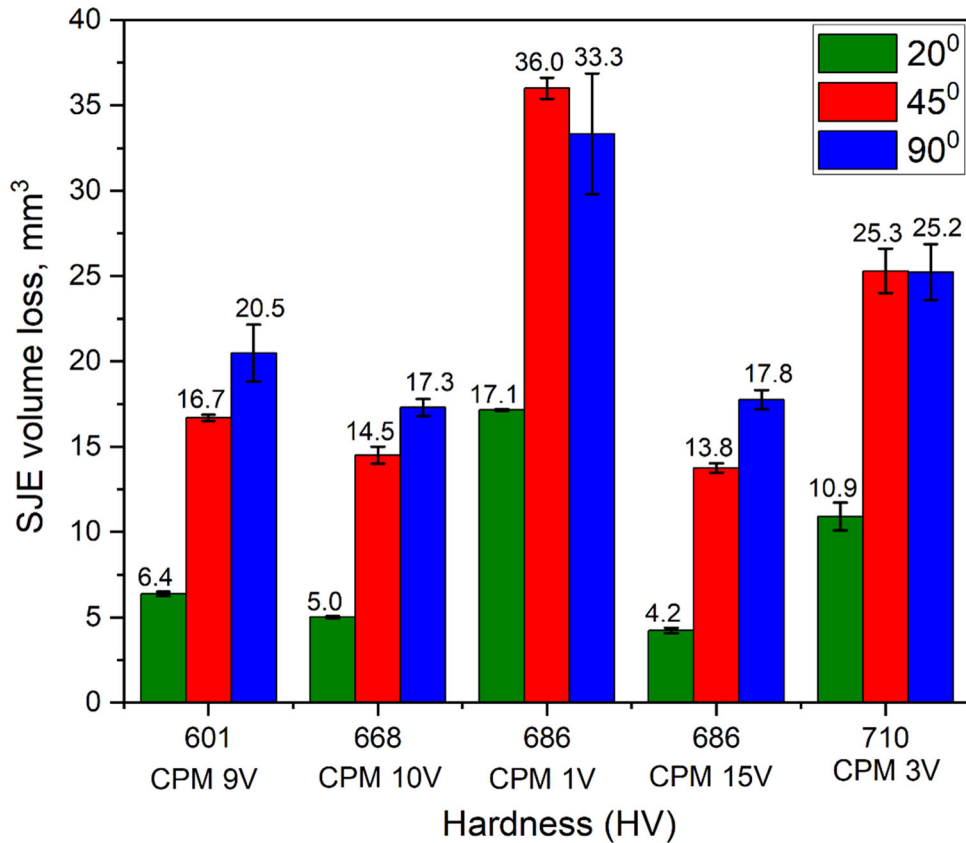
Fig. 8 Relationship between SJE wear volume loss and hardness (HV) for the CPM yV tool steels

Table 4 Material hardness (H_m), minimum abrasive hardness (H_a), maximum abrasive hardness (H_a), minimum H_a/H_m, maximum H_a/H_m and average between max and min H_a/H_m calculated for the CPM yV tool steels and silica erodent

Alloy	Material hardness , H_m	Minimum abrasive hardness, H_a	Minimum, H_a/H_m	Maximum abrasive hardness, H_a	Maximum, H_a/H_m	Average max-min, H_a/H_m
CPM 1V	704	652	0.93	900	1.28	1.10
CPM 3V	697	652	0.94	900	1.29	1.11
CPM 9V	582	652	1.12	900	1.55	1.33
CPM 10V	676	652	0.96	900	1.33	1.15
CPM 15V	718	652	0.91	900	1.25	1.08
Average	675	652	0.97	900	1.34	1.16
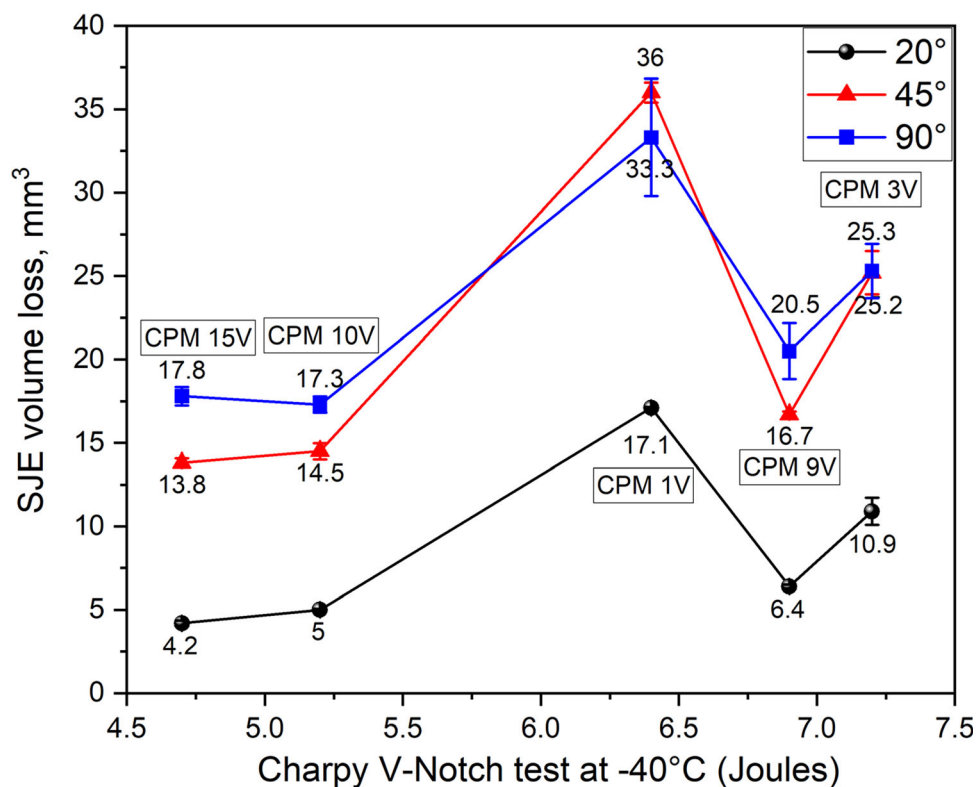
Fig. 9 Relationship between SJE wear volume loss and impact toughness (Charpy V-notch test at − 40 °C) for the CPM yV tool steels

contrary to the observed results in this study. It should be noticed that the Z-curve relationship was obtained based on two-body abrasion tests. In two-body abrasion, the hard carbide particles and the matrix are worn at similar rate by the penetrating abrasive; thus, the overall material wear rate is mainly determined by the abrasive penetration depth which is controlled by the material hardness. Therefore, the two-body abrasion resistance is strongly affected by the macroscale material hardness.

The material loss rate at the same penetration depth (same penetration depth) may be different for materials with or without

secondary hard particles (e.g., carbides), depending on the wear damage mechanisms for the hard secondary particles. For erosion, limited studies have been found regarding the effect of hardness ratio, H_a/H_m, between the abrasive and the material (Ref 15). Zambrano et al. (Ref 15) studied the effect of H_a/H_m ratio on the erosion of selected steels treated to different hardness values using three erodent particles (alumina, silica and garnet). It was found that the erosion can be classified into three different regimes based on the H_a/H_m ratios. Thus, erosion is mild/moderate when H_a/H_m ratio is below 2.60 (where silica sand and garnet and erosion were used as the erodent). Erosion is in the
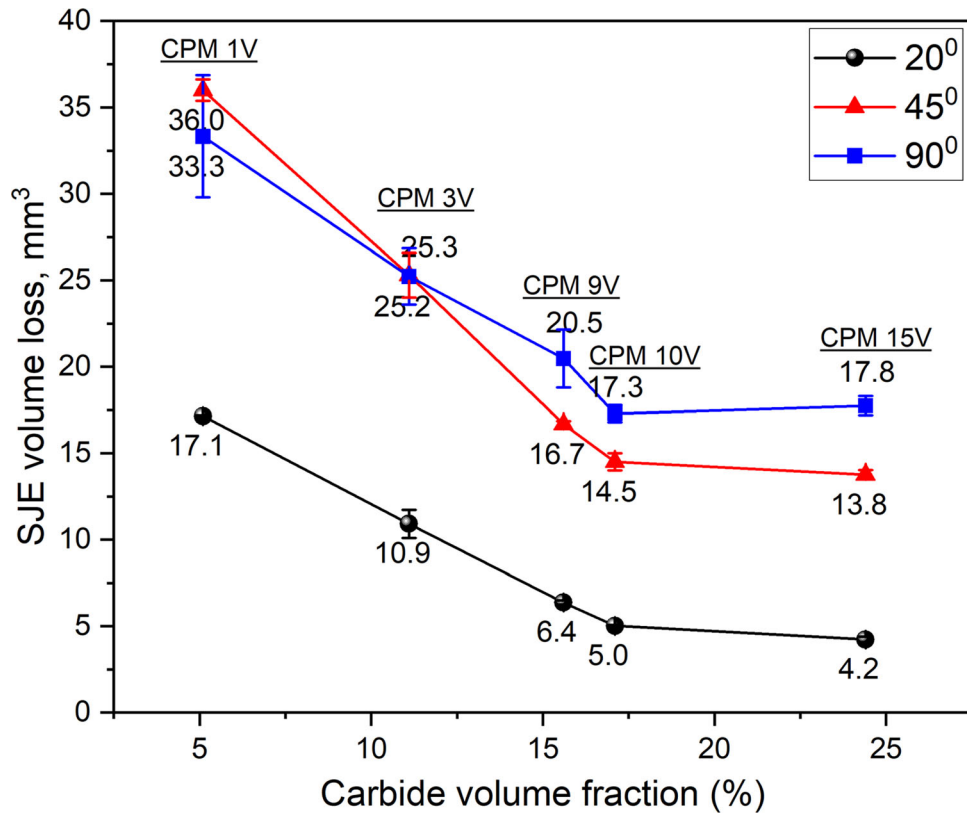
Fig. 10 Relationship between SJE wear volume loss and CVF for the CPM yV tool steels
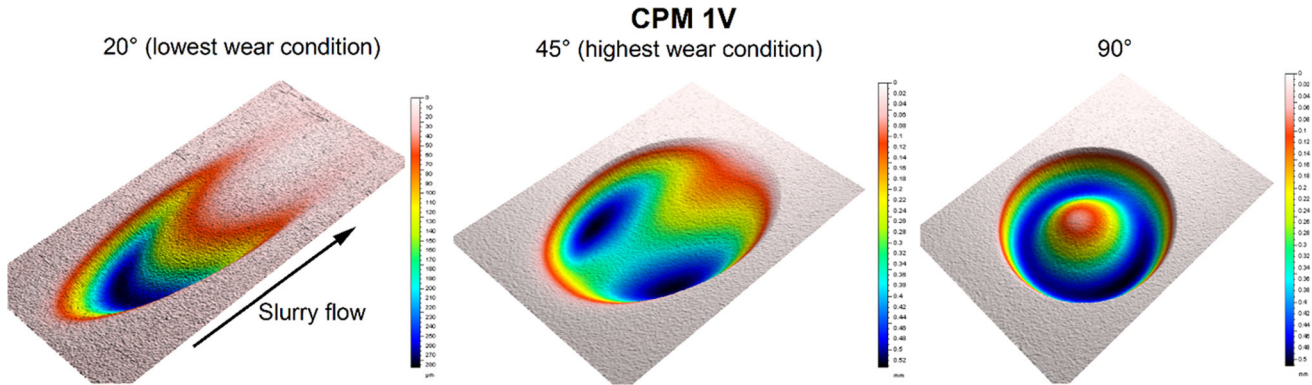

Fig. 11 Laser profilometry image of the wear scar of the CPM 1V steel at different impingement angles: 20° (left), 45° (center) and 90°(right), respectively

high-rate regime for H_a/H_m ratios greater than 2.94 when using alumina as the erodent. There is a transition erosion regime for H_a/H_m ratios between 1.86 and 3.10 where the erosion rate is in the intermediate level between that for the mild and for the severe erosion regimes. It was noticed that within each of the three erosion regimes, material hardness has no effect on the erosion rate, including in the transition regime, and other factors influence the erosion wear transition such as the number of particles hitting the surface and the fracture toughness of the erodent. The H_a/H_m ratios for the CPM yV steels in the current study (0.93 and 1.55) fall within the moderate erosion regime by Zambrano et al. (Ref 15) (≤ 2.60 using silica as the erodent). The results from both studies agree well.

The difference between two-body abrasion and erosion in terms of the relative hardness (H_a/H_m ratio) effect may be related to the difference in wear processes. During erosion of inhomogeneous materials such as the CPM yV steels, the matrix is first preferentially eroded, and then, the material loss rate reaches some steady state. The steady-state material loss rate will be dominated by the wear of the protruding carbide particles. Therefore, the carbide volume fraction rather than the overall hardness of the material is the dominant affecting factor on the erosion resistance of the CPM yV steels. On the other hand, in two-body abrasion, the hard carbide particles and the matrix are worn simultaneously by the fixed abrasive particles. Wear rate is mainly controlled by the penetration depth of the abrasive particle which is determined by the material hardness. Therefore, the macroscale material hardness is very important in affecting the two-body abrasion resistance.
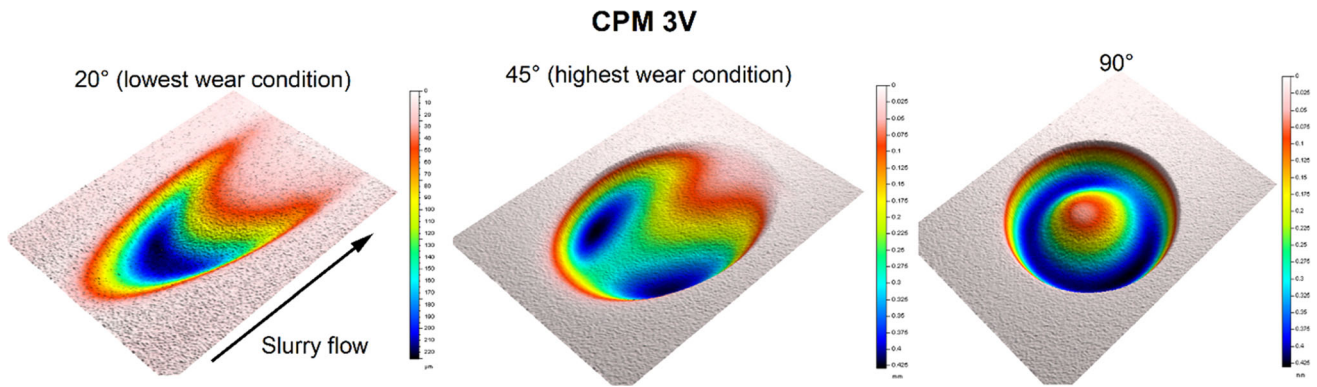
CPM 3V

Fig. 12 Laser profilometry image of the wear scar of the CPM 3V steel at different impingement angles: 20° (left), 45° (center) and 90°(right), respectively
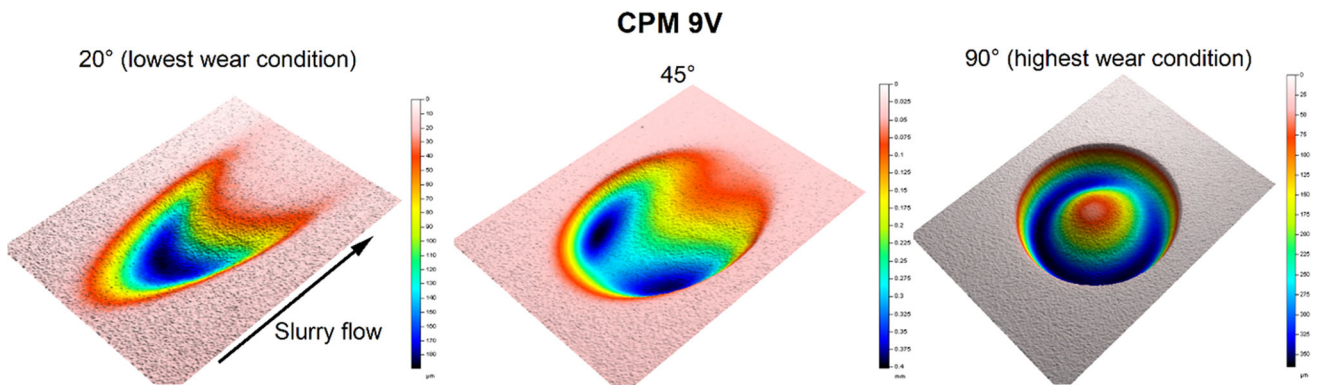
CPM 9V

Fig. 13 Laser profilometry image of the wear scar of the CPM 9V steel at different impingement angles: 20° (left), 45° (center) and 90°(right), respectively
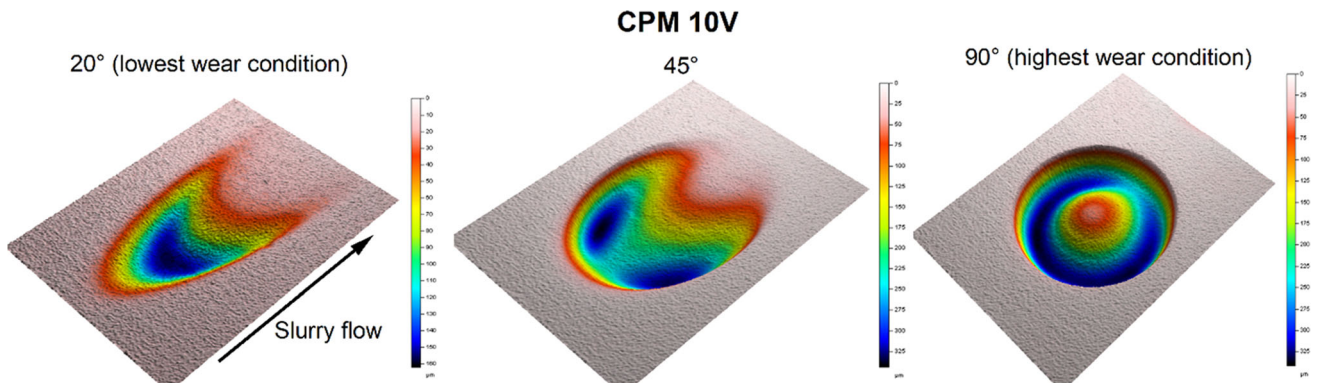
CPM 10V

Fig. 14 Laser profilometry image of the wear scar of the CPM 10V steel at different impingement angles: 20° (left), 45° (center) and 90°(right), respectively

3.2.3 The Role of Impact Toughness (Charpy Tests − 40 °C). Figure 9 shows the SJE wear loss versus impact toughness for each steel. No satisfactory correlation was found between impact toughness and SJE resistance. In other words, increasing/decreasing the steel's toughness does not lead to a consistent decrease/increase in the SJE resistance. It is important to note that a Kruskal–Wallis statistical test was used with an 85% confidence level to determine whether or not the mean Charpy values (Table 2) were statistically significant or not. The Kruskal–Wallis test does not assume normal distribution of the data and can be used to determine if there are statistically significant differences between two or more groups. Based on this statistical test, it was determined that the difference in the mean Charpy test values among the steels is significant (at the 85% confidence level). Thus, for instance, the CPM 9V tool has a higher impact toughness than the CPM 1V and CPM 3V. However, its erosion behavior is brittle-like based on Figure 7. Thus, the impact toughness of the steels cannot be used to explain the ductile–brittle behaviors for the different steels during slurry erosion. Therefore, other factors than hard-
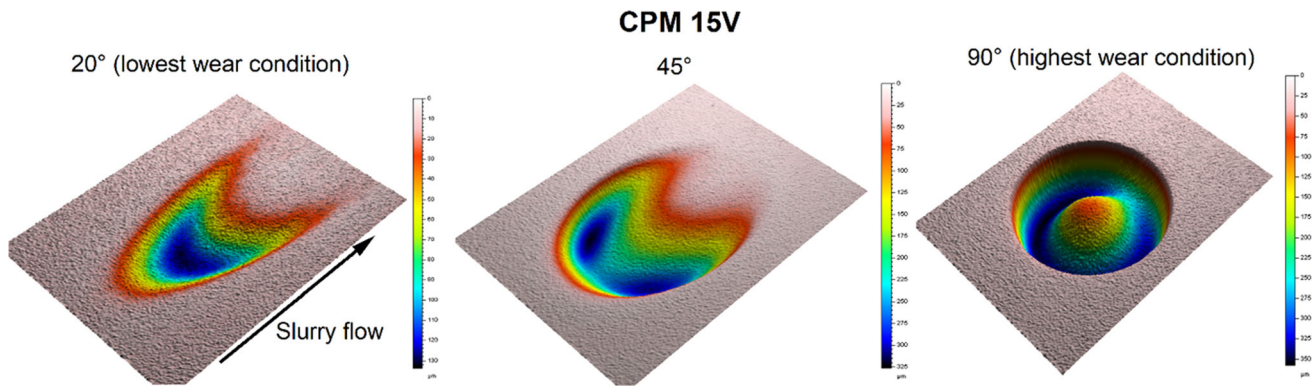
CPM 15V

20° (lowest wear condition)   45°   90° (highest wear condition)

Slurry flow

Fig. 15 Laser profilometry image of the wear scar the CPM 15V steel at different impingement angles: 20° (left), 45° (center) and 90°(right), respectively

Table 5 Maximum wear scar depths (μm) at different impingement angles of the studied steels determined from Figure 11, 12, 13, 14 and 15

Alloy	Impingement angle, °		
	20°	45°	90°
CPM 1V	280	520	505
CPM 3V	220	425	420
CPM 9V	180	355	350
CPM 10V	160	325	325
CPM 15V	130	325	350

ness/toughness need to be considered which will be discussed below. The fracture surfaces of the CPM yV tool steels after testing at –40°C are shown in supplementary information (Figure S1, S2, S3, S4 and S5).

3.2.4 The Role of the Carbide Volume Fraction .   The relationship between the SJE volume loss and carbide volume fraction (CVF) for the studied steels is shown in Figure 10. A good correlation between SJE volume loss and CVF is observed: An increase in carbide volume fraction results in a decrease in volume loss for all impingement angles. The CPM 15V steel has the highest CVF and displayed the best erosion performance. It can be seen here that the CVF (Figure 10) has a more preponderant role than hardness (Figure 8). For instance, the contrasting erosion behavior of the CPM 1V and CPM 15V steels despite having the same hardness shows that the matrix by itself is not able to withstand the erosion conditions, and the reinforcement particles help to prevent further damage. This will be discussed in detail in sect. 3.4.

3.2.5 Laser Profilometry. Figure 11, 12, 13, 14, 15 shows the 3D morphology of wear scars of the CPM 1V to CPM 15V tool steels after being tested at different impingement angles.

At 20°, the wear scar of the CPM yV tool steels show a comet shape, where most wear is located at the beginning of the contact between the slurry flow and specimens' surface. On the other hand, at 45° the wear scar shape is oval with double sinks; these two "valleys" are located one beside the other, which is probably mainly caused by the nature of the slurry flow and the predominant ductile/brittle behavior of the material. On the other hand, at 90°, the morphology of the wear scars appears as

a circular valley. The different maximum depths determined at each impingement angle for the studied tool steels are summarized in Table 5. The general trend of wear scar depth as a function of CVF agrees fairly well with the SJE volume loss results in Figure 10.

Some degree of variations can be observed between the different grades of the tool steels. For example, at the 45° impingement angle, the CPM 1V steel scar (Figure 11) shows a clear oval outline/contour along the scar edge; however, for the CPM 15V steel (Figure 15) the outline of the scar edges is not completely oval, but has comet-shaped tails something similar to that formed at the 20° impingement angle. Further research is required to elucidate the reasons for such difference. Finally, it can be observed that the geometry of the wear scars obtained at 20°, 45° and 90° are in overall consistent with those reported using CFD simulations (Ref 27) and erosion experiments (Ref 28) for a CA6NM stainless steel. However, the shape of the wear scars resulting from erosion is greatly influenced by the materials being tested, fluid velocity and particularly the size of the particles. Smaller particles are more likely to follow the flow of the fluid, while larger particles tend to follow the path defined by the jet at the outlet due to their greater inertia (Ref 27).

3.2.6 Wear Micromechanisms .   Wear scars after the SJE testing were examined using a SEM with secondary and backscattered electrons in order to comprehend the dominant wear mechanisms and the different wear behaviors of the CPM yV steels. The secondary electrons imaging provides a topographical information while the backscattered electrons images provide better chemical compositional contrast that helps to differentiate more clearly the role of VC particles from the matrix. The SEM images were taken from the deepest points as highlighted in blue color in sect. 3.2.5 for each steel (Figure 11, 12, 13, 14 and 15), i.e., the areas of highest wear rate. Some typical SEM images of wear scars are presented in Figure 16, 17, 18, 19 and 20 for CPM 1V-CPM 15V steel specimens, respectively. Each figure includes SEM images for two impingement angles corresponding to the lowest erosion loss and the highest erosion loss, respectively, i.e., 20° (lowest erosion loss) for all the steels and 45° for CPM 1V and CPM 3V (Figure 16, 17) and 90° for CPM 9-CPM 15 (Figure 18, 19 and 20).

Figure 16 for CPM 1V steel, at the impingement angle of 20°, shows a high degree of microcutting and lateral deformation around the grooves (microplowing) are observed. In
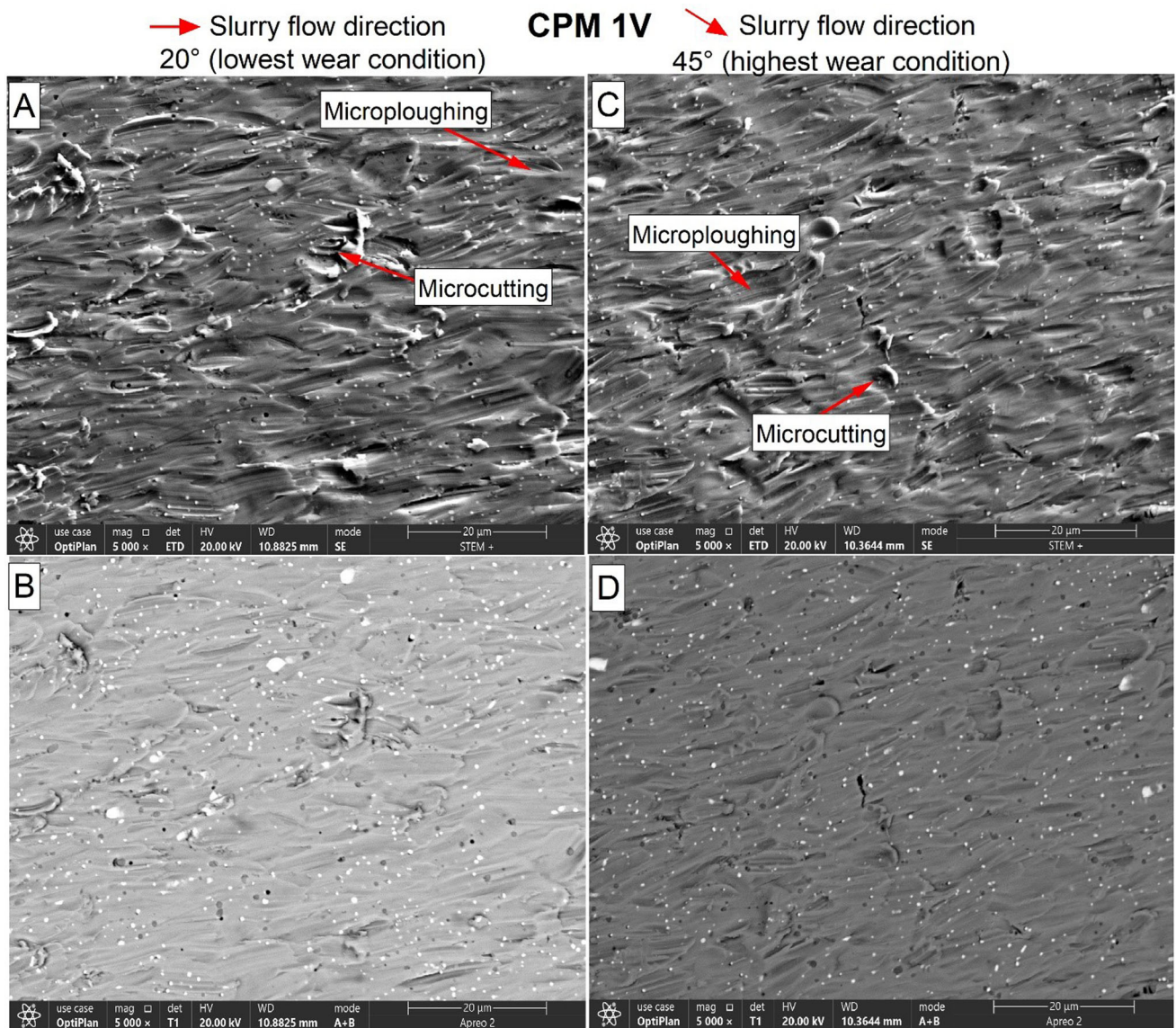
Fig. 16 Scanning electron microscopy images of the wear scars of the CPM 1V steel tested at (a, b) 20° and (c, d) 45° impingement angle using secondary electrons and backscattered electrons, respectively

contrast, at 45° where the highest erosion loss was observed, the degree of microcutting and lateral deformation around the grooves (microplowing) is much higher than at 20°.

The CPM 3V steel wear surface (Figure 17) presented similar features to that observed in CPM 1V wear scars. At 20°, a medium–high degree of microcutting and lateral deformation around the grooves (microplowing) are observed. In contrast, the degree of microcutting and lateral deformation around the grooves (microplowing) is increased at the impingement angle of 45° as compared with that at 20°.

For specimen CPM 9V and henceforth, the highest wear condition changed from 45° to 90° and hence the wear mechanism. This tacitly means the material behavior is changing from ductile to more brittle with increase in the vanadium concentration (Figure 7). At 20° (Figure 18), a medium–high degree of microcutting and lateral deformation around the grooves (microplowing) are observed. The depth of cutting is much less than in CPM 1V and CPM 3V (Figure 16, 17). In contrast, at 90°, a medium degree of microcutting, with

low degree of microplowing occurred. Some pittings were noticed in the scar.

Figure 19 displays wear surface of the CPM 10V. After testing at impingement angle of 20°, the wear scar surface is very smooth with a low degree of microcutting mechanism. Standout of fine VC protecting the matrix was noticeable. At 90°, very small number of shallow microcutting marks was observed. Pitting becomes more widespread than in the case of CPM 9V.

Finally, the 20° SJE test scar for the CPM 15V steel (Figure 20) shows further reduced degree of microcutting but more apparent standout effect of the VC carbides which protect the steel matrix from wear by microcutting. At 90°, the wear surface shows some similarities to the CPM 10V (Figure 19) in that the degree of microcutting is very low, but pitting is even more widespread.
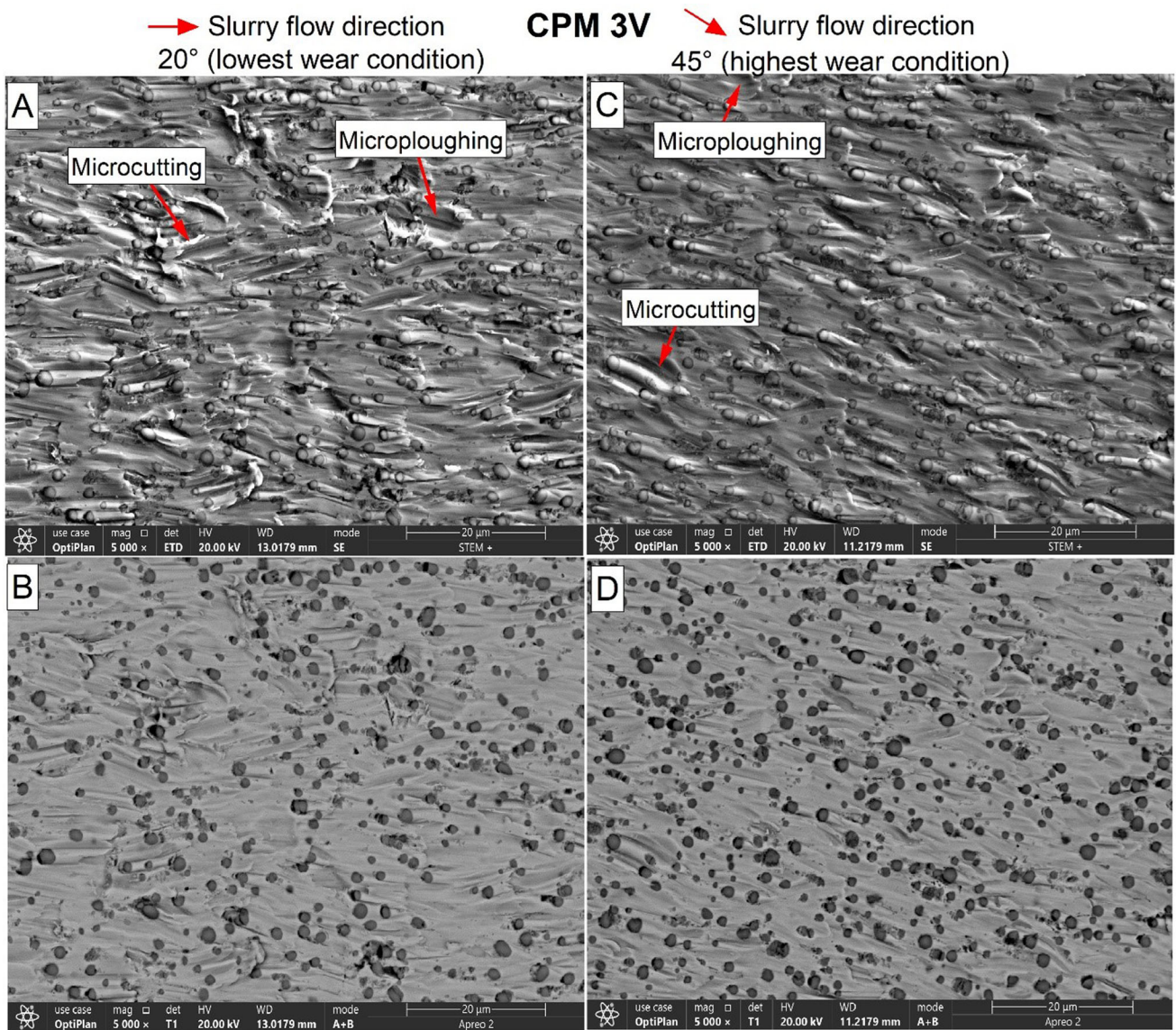
Fig. 17 Scanning electron microscopy images of the wear scars of the CPM 3V steel tested at (a, b) 20° and (c, d) 45° impingement angle using secondary electrons and backscattered electrons, respectively

3.3 Discussion

Figure 7 shows that the erosion volume loss increases with the increase in the impingement angle from 20 to 90° for the ASTM A532 white iron and for CPM steels with CVF higher than ∼ 15% (CPM 9V, 10V and 15V). This indicates a brittle erosion behavior for these materials under the SJE conditions. On the other hand, the CPM 1 V and CPM 3 V (lower CVF than ∼ 15%) displayed a ductile-like behavior. In other words, there erosion behavior transition from more ductile to more brittle occurred at a CVF value of about 15%. It is important to notice that once a critical value of CVF is reached, believed to be around 15% in the current study, no further improvement from the wear point of view can be achieved. This is most likely because the mean free path is not further decreased (see Table 2) by increasing the CVF above this critical value as the VC particle size increases at high CVF. The results of the wear scar examination align with this observation, which shows that microcutting and microplowing is dominant for CPM 1V

(Figure 16) and CPM 3V (Figure 17) at the different impingement angles, typical of erosion of ductile materials.

An increase in CVF in CPM yV tool steels has two different impacts on the erosion behavior. Firstly, SEM analysis of the worn surfaces revealed that as CVF increases, the grooving caused by microcutting and/or microplowing becomes less pronounced (Figure 16, 17, 18, 19 and 20). This might be largely ascribed to the hardness of VC particles which are harder than the abrasive particles. During the erosion process, the hard and fine VC particles will interrupt and reduce the length of the continuous scratching/grooving (microcutting or microplowing) of the wear surface and shield the matrix from wear. Evidence of this is provided through the wear scars in Figure 16, 17, 18, 19 and 20. This effect is expected to reduce erosion loss of the CMP yV steels with increase in the CVF. As shown in Figure 10, the SJE resistance (the inverse of erosion loss) of the CPM yV steels increases significantly with the increase in the CVF regardless of the bulk hardness. Similar results were observed recently for CPM steels tested under
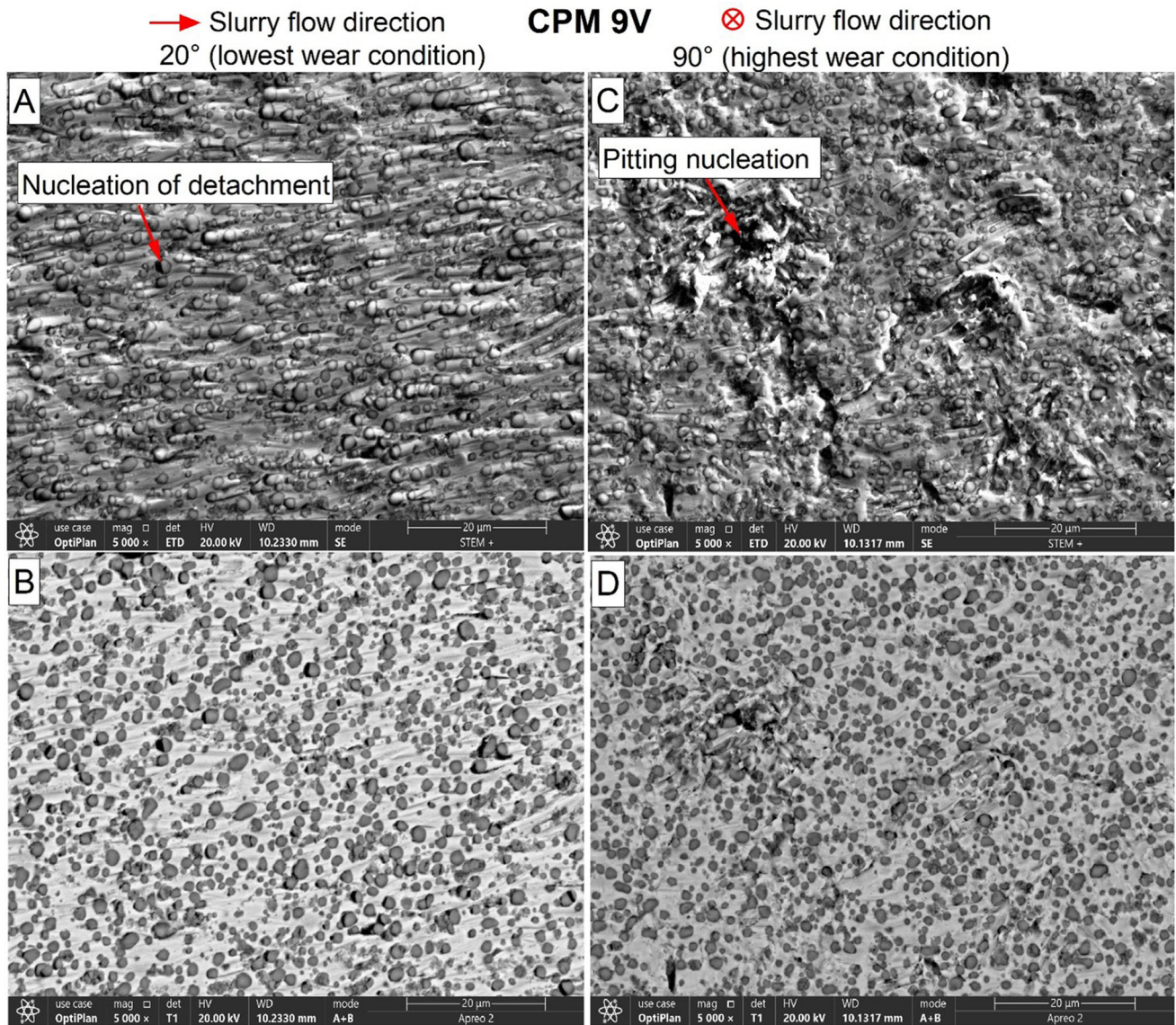
Fig. 18 Scanning electron microscopy images of the wear scars of the CPM 9V steel tested at (a, b) 20° and (c, d) 90° impingement angle using secondary electrons and backscattered electrons, respectively. The symbol ⊗ means that the flow direction goes into the plane (perpendicular to the plane).

scoring erosion conditions (Ref 10). On the other hand, with the increase in CVF and the correspondingly reduced contribution of erosion loss by grooving (cutting or plowing), the same location of the wear surface will be impacted for an extended period of time prior to being removed. As a result, the contribution of microfatigue wear mechanism on total material loss increases. Obviously, the relative contribution of impact fatigue mechanism will be more apparent at higher impingement angles where the normal impact component of the erodent particle energy is much higher. Material loss due to the microfatigue mechanism is usually related to brittle erosion behavior. Thus, this eventually leads to brittle erosion behavior for the high-CVF steels. The higher tendency for microcracks to initiate and spread along the carbide/matrix boundary in steels with high carbide volume fraction leads to the formation of pitting-like features on the wear surface, as observed in Figure 18 and 20.

Finally, it is interesting to notice that CPM 9V, 10V and 15V steels displayed noticeably better erosion resistance than the ASTM A532 IIIA Cr white cast iron that is widely used in industrial slurry handling equipment (Figure 7); the erosion resistance of CPM 15V is 2.4, 1.5 and 1.6 times of the Cr white iron at 20°, 45° and 90°, respectively. This finding is significant for industrial applications because, according to our experience with the Canadian oil sands mining industry, although the magnitude of erosion resistance improvement in the actual service life in industrial applications may not be the same as derived from the SJE test results in the laboratory, these results do indicate that the CPM yV steels hold great promise to perform significantly better than the ASTM A532 IIIA Cr white irons in slurry handling applications at least where the dominant erodent particle sizes are not far from 200 to 300 μm. It has to be pointed out that tribo-corrosion synergistic effect is not reflected in the SJE test which must be taken into
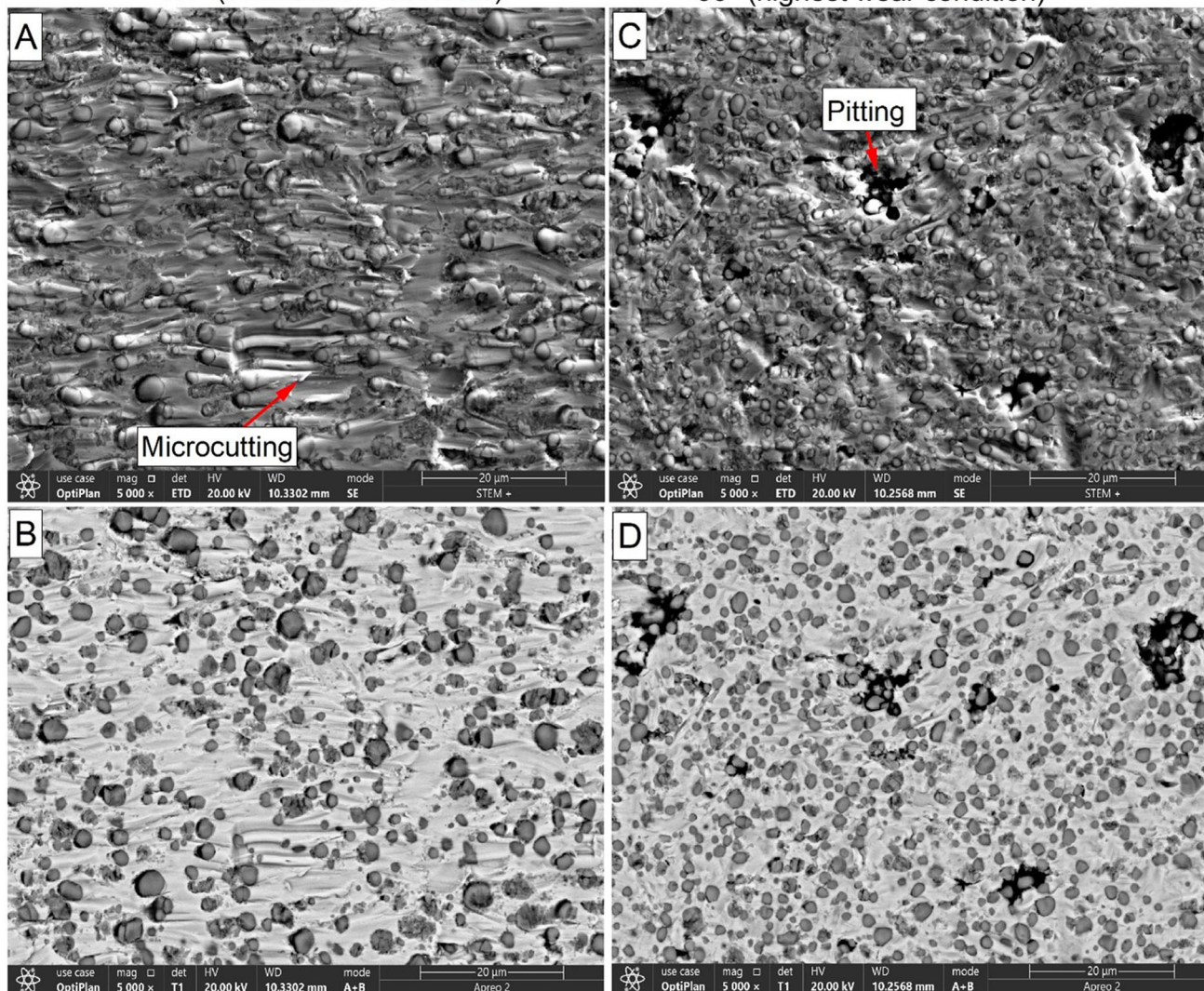
Fig. 19 Scanning electron microscopy images of the wear scars of the CPM 10V steel tested at (a, b) 20° and (c, d) 90° impingement angle using secondary electrons and backscattered electrons, respectively. The symbol ⊗ means that the flow direction goes into the plane (perpendicular to the plane).

account when selecting materials for applications involving corrosive media.

The factors contributing to a high erosion resistance of the CPM yV steels, particularly to the ones with higher VC (y = 9, 10, 15), as compared with the Cr white cast iron are not immediately apparent and is a subject for further study. The characteristics of these two classes of materials are completely different. Therefore, it is hard to make direct comparisons. The CVF (the massive eutectic M_7C_3 carbide, not including the fine secondary carbide in the matrix) in the ASTM A532 IIIA Cr white irons is typically in the range of 25-32% which is considerably higher than the volume fractions of VC particles in the CPM yV steels. The superior erosion resistance of CPM yV steels with high CVF may be attributed to the close proximity of the carbides and the uniform dispersion of fine vanadium carbides. This arrangement ensures that the vanadium carbide particles primarily bear the contact stress at the boundary between the erodent and the worn surface, safe-

guarding the surface against severe wear such as deep penetration or cutting. On the other hand, although the Cr white cast iron has higher CVF, erodent particles can more easily penetrate the matrix between the large (massive) eutectic carbides and cause preferential erosion loss of the matrix, leading to more rapid damage to the carbide and reducing the effectiveness of wear protection by these carbides. In the meantime, the relatively large bulky/massive M_7C_3 carbide in the Cr white cast iron may be more prone to microfracture (microchipping or microfatigue) damages by the repeated impact of erodent which is not expected for the fine VC in the CPM yV steels. Thus, even though the CPM yV steels contain lower CVF, they displayed very good erosion resistance under the current test conditions as compared with the Cr white cast iron. It is important to point out that the results of this work are limited to tool steels containing VC particles with similar microstructure. There are some aspects that still need to be investigated such as the detailed characterization of the erosion
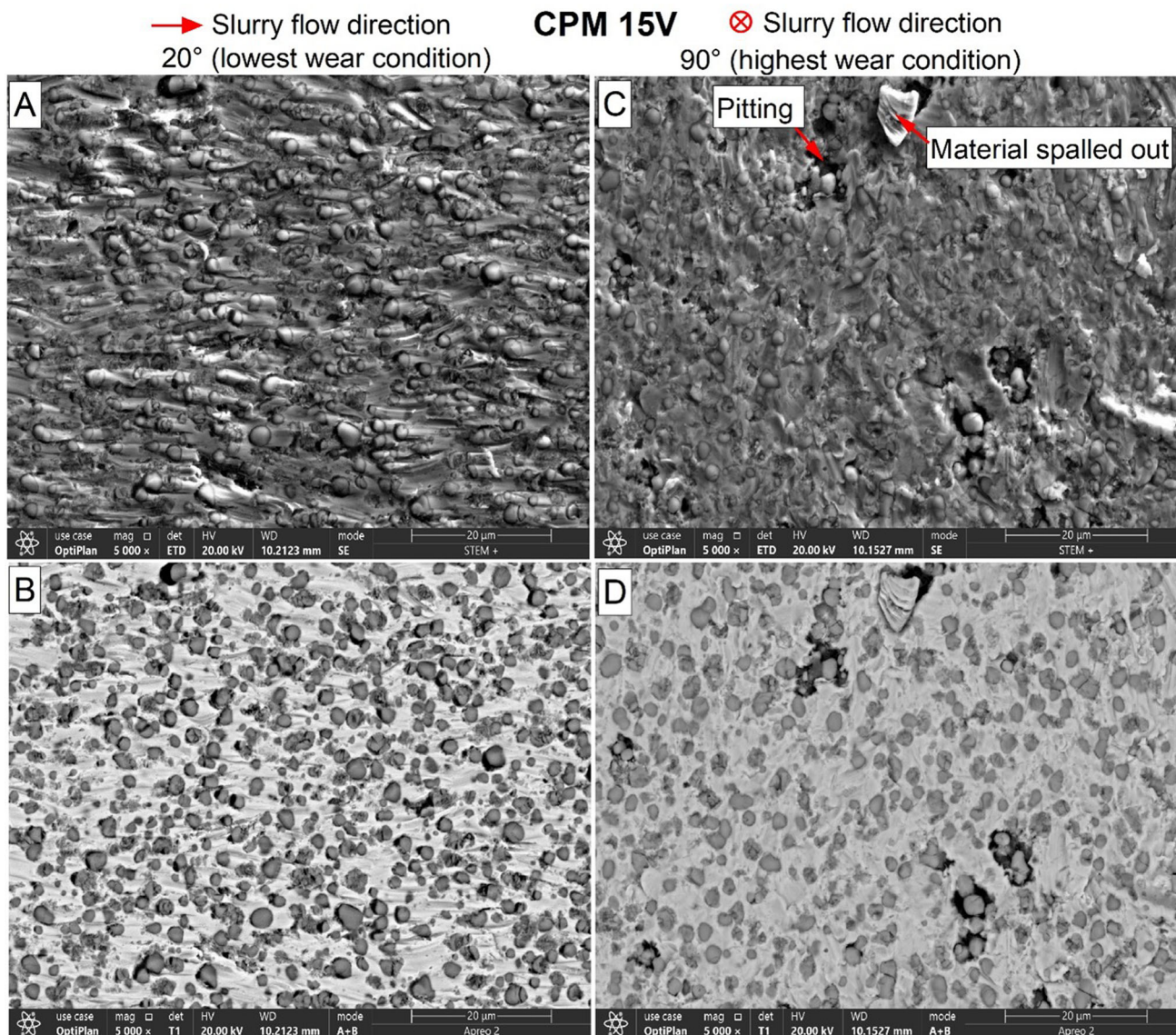
Fig. 20 Scanning electron microscopy images of the wear scars of the CPM 15V steel tested at (a, b) 20° and (c, d) 90° impingement angle using secondary electrons and backscattered electrons, respectively. The symbol ⊗ means that the flow direction goes into the plane (perpendicular to the plane).

behavior at more impingement angles, as well as the effect of erodent particle size on erosion of the CPM yV steels.

4. Conclusions

The slurry jet erosion (SJE) behavior of five CPM yV (x = 1, 3, 9, 10, 15) tool steels was studied. The results support the following conclusions:

- The wear response of these tool steels subjected to SJE conditions cannot be solely attributed to their bulk hardness nor their Charpy energy.
- Irrespective of the impingement angle, increasing the carbide volume fraction (CVF) enhances the ability to withstand erosion wear up to 9% V. Further increase in V contend did not resulted in significant wear resistance

improvement.
- The contribution of microcutting and microplowing wear mechanisms to erosion loss of these steels decreases as the CVF increases.
- With a proper control of the process variables/heat treatments, the CPM 15V has potential to perform better than the alloys with lower vanadium content.
- The CPM 9 V, 10 V and 15 V steels exhibited significantly superior slurry erosion resistance compared to the ASTM A532 IIIA Cr white cast iron, which is a predominant material in industrial slurry handling equipment.

Acknowledgments

Open Access

References

1. F.G.S. Bastidas and C.P. Bergmann, Jet Slurry Erosion of CERMET Nano-Coatings Obtained by HVOF, *Technological Applications of Nanomaterials, A*. K. Alves Ed., Springer International Publishing, Cham, 2022, p 1–33

2. V. Javaheri, D. Porter, and V.-T. Kuokkala, Slurry Erosion of Steel – Review of Tests, Mechanisms and Materials, *Wear*, 2018, **408–409**, p 248–273.

3. R.J. Chung, J. Jiang, C. Pang, B. Yu, R. Eadie, and D.Y. Li, Erosion-Corrosion Behaviour of Steels used in Slurry Pipelines, *Wear*, 2021, **477**, p 203771.

4. S.H. Wang, J.Y. Chen , and L. Xue, A Study of the Abrasive Wear Behaviour of Laser-Clad Tool Steel Coatings, *Surf. Coat. Technol.*, 2006, **200**(11), p 3446–3458.

5. J. Chen, S. Wang , and L. Xue, Dry Sliding Wear of Laser-Clad High-Vanadium Crucible Powder Metallurgy (CPM) 3V, 9V, and 15V Tool Steel Coatings, *Metallogr. Microstruct. Anal.*, 2019, **8**(5), p 693–704.

6. R.A. Poggie and J.J. Wert, The Influence of Surface Finish and Strain Hardening on Near-Surface Residual Stress and the Friction and Wear Behavior of A2, D2 and CPM-10V Tool Steels, *Wear*, 1991, **149**(1), p 209–220.

7. R.M.M. Riofano, L.C. Casteletti, L.C.F. Canale and G.E. Totten, Improved Wear Resistance of P/M tool Steel Alloy with Different Vanadium Contents After Ion Nitriding, *Wear*, 2008, **265**(1), p 57–64.

8. P. Kattire, S. Paul, R. Singh , and W. Yan, Experimental Characterization of Laser Cladding of CPM 9V on H13 Tool Steel for Die Repair Applications, *J. Manuf. Process.*, 2015, **20**, p 492–499.

9. O.A. Zambrano, J. Gholipour, P. Wanjara , and J. Jiang, Linear Friction Welding of Abrasion Resistant CPM 15V Tool Steel to an Alloyed Carbon Shovel-Tooth Steel, *J. Manuf. Mater. Process.*, 2023, **7**(2), p 51.

10. O.A. Zambrano and J. Jiang, The Effect of VC Content on the Scouring Erosion Resistance of Tool Steels, *Wear*, 2023, **520–521**, p 204669.

11. A. Bansal, J. Singh , and H. Singh, Investigating Slurry Erosion Behavior of a Hydro-Machinery Steel under Various Impingement Variables, *Mater. Today Proc.*, 2021, **41**, p 795–800.

12. K.-H. Zum Gahr, *Microstructure and Wear of Materials*, Elsevier, London, 1987

13. I. Finnie, Erosion of Surfaces by Solid Particles, *Wear*, 1960, **3**(2), p 87–103.

14. J.G.A. Bitter, A Study of Erosion Phenomena Part I, *Wear*, 1963, **6**(1), p 5–21.

15. O.A. Zambrano, D.S. García, S.A. Rodríguez , and J.J. Coronado, The Mild-Severe Wear Transition in Erosion Wear, *Tribol. Lett.*, 2018, **66**(3), p 95.

16. International, A., *E140-12B(2019)1 Standard Hardness Conversion Tables for Metals Relationship Among Brinell Hardness, Vickers Hardness, Rockwell Hardness, Superficial Hardness, Knoop Hardness, Sclerescope Hardness, and Leeb Hardness*. 2019: West Conshohocken, PA

17. J.S. Rodriguez, J.F. Duran, Y. Aguilar, G.A.P. Alcazar, R.M. Souza and O.A. Zambrano, Effect of Aluminum Content on the Dynamic Recrystallization of Fe18MnxAl0.74C Steels During Hot-Forging Treatments, *Metall. Mater. Trans. A*, 2022, **53**(8), p 2961–2976.

18. O.A. Zambrano and R.E. Logé, Dynamic Recrystallization Study of a Fe-Mn-Si Based Shape Memory Alloy in Constant and Variable Thermomechanical Conditions, *Mater. Charact.*, 2019, **152**, p 151–161.

19. O.A. Zambrano, J. Valdés, Y. Aguilar, J.J. Coronado, S.A. Rodríguez and R.E. Logé, Hot Deformation of a Fe-Mn-Al-C Steel Susceptible of κ-Carbide Precipitation, *Mater. Sci. Eng., A*, 2017, **689**, p 269–285.

20. O.A. Zambrano, G. Tressia and R.M. Souza, Failure Analysis of a Crossing Rail Made of Hadfield Steel after Severe Plastic Deformation Induced by Wheel-Rail Interaction, *Eng. Fail. Anal.*, 2020, **115**, p 104621.

21. J.F. Durán, G.A. Pérez, J.S. Rodríguez, Y. Aguilar, R.E. Logé and O.A. Zambrano, Microstructural Evolution Study of Fe-Mn-Al-C Steels Through Variable Thermomechanical Treatments, *Metall. and Mater. Trans. A.*, 2021, **52**(11), p 4785–4799.

22. J.G.A. Bitter, A Study of Erosion Phenomena: Part II, *Wear*, 1963, **6**(3), p 169–190.

23. I. Finnie, Some Observations on the Erosion of Ductile Metals, *Wear*, 1972, **19**(1), p 81–90.

24. I. Finnie, J. Wolak and Y. Kabil, Erosion of Metals by Solid Particles, *J. Mater.*, 1967, **2**(3), p 682–700.

25. K.H.Z. Gahr, Wear by Hard Particles, *Tribol. Int.*, 1998, **31**(10), p 587–596.

26. O.A. Zambrano, J.A. Gómez, J.J. Coronado and S.A. Rodríguez, The Sliding Wear Behaviour of Steels with the Same Hardness, *Wear*, 2019, **418–419**, p 201–207.

27. R.D. Aponte, L.A. Teran, J.A. Ladino, F. Larrahondo, J.J. Coronado and S.A. Rodríguez, Reprint of '"Computational Study of the Particle Size Effect on a Jet Erosion Wear Device,"' *Wear*, 2017, **376–377**, p 526–532.

28. S.A. Romo, J.F. Santa, J.E. Giraldo and A. Toro, Cavitation and High-Velocity Slurry Erosion Resistance of Welded Stellite 6 Alloy, *Tribol. Int.*, 2012, **47**, p 16–24.